

# Effect of Surface Modification on Water Adsorption and Interfacial Mechanics of Cellulose Nanocrystals

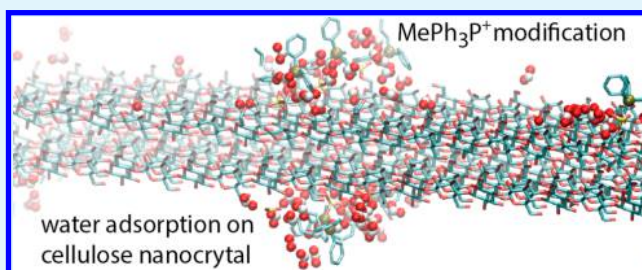
Zonghui Wei,<sup>†</sup> Robert Sinko,<sup>‡</sup> Sinan Keten,<sup>‡,§</sup> and Erik Lijten<sup>\*,†,||,⊥,#</sup>

<sup>†</sup>Graduate Program in Applied Physics, <sup>‡</sup>Department of Mechanical Engineering, <sup>§</sup>Department of Civil and Environmental Engineering, <sup>||</sup>Department of Materials Science and Engineering, <sup>⊥</sup>Department of Engineering Sciences and Applied Mathematics, and <sup>#</sup>Department of Physics and Astronomy, Northwestern University, Evanston, Illinois 60208, United States

## Supporting Information

**ABSTRACT:** With increasing environmental concerns about petrochemical-based materials, the development of high-performance polymer nanocomposites with sustainable filler phases has attracted significant attention. Cellulose nanocrystals (CNCs) are promising nanocomposite reinforcing agents due to their exceptional mechanical properties, low weight, and bioavailability. However, there are still numerous obstacles that prevent these materials from achieving optimal performance, including high water adsorption, poor nanoparticle dispersion, and filler properties that vary in response to moisture. Surface modification is an effective method to mitigate these shortcomings. We use computational approaches to obtain direct insight into the water adsorption and interfacial mechanics of modified CNC surfaces. Atomistic grand-canonical Monte Carlo simulations demonstrate how surface modification of sulfated Na-CNCs impacts water adsorption. We find that methyl(triphenyl)phosphonium (MePh<sub>3</sub>P<sup>+</sup>)-exchanged CNCs have lower water uptake than Na-CNCs, supporting experimental dynamic vapor sorption measurements. The adsorbed water molecules show orientational ordering when distributed around the cations. Steered molecular dynamics simulations quantify traction–separation behavior of CNC–CNC interfaces. We find that exchanging sodium for MePh<sub>3</sub>P<sup>+</sup> effectively changes the surface hydrophilicity, which in turn directly impacts interfacial adhesion and traction–separation behavior. Our analysis provides guidelines for controlling moisture effects in cellulose nanocomposites and nanocellulose films through surface modifications.

**KEYWORDS:** cellulose nanocrystals, surface modification, computer simulations, water adsorption, interfacial properties



## 1. INTRODUCTION

Cellulose, an organic polysaccharide, serves many roles in natural systems but most notably is the major structural component of plant matter, leading it to be the most abundant renewable polymer found in nature.<sup>1</sup> When bulk cellulosic materials, such as wood pulp, are subject to chemical, mechanical, and/or enzymatic treatment,<sup>2–4</sup> the amorphous regions of cellulose microfibrils are predominantly hydrolyzed. Upon further processing, the remaining microfibrils break into shorter cellulose nanocrystals (CNCs) that are highly crystalline with a high aspect ratio.<sup>5</sup> Within this crystal structure, cellulose chains are closely packed together by van der Waals interactions and an extensive network of hydrogen bonds that exist both within (intra-chain) and among (inter-chain) linear cellulose chains.<sup>6,7</sup> CNCs exhibit many appealing intrinsic properties, including nanoscale dimensions, high aspect ratio, high biodegradability and bioavailability, low density, and exceptional mechanical strength.<sup>8</sup> Thus, they possess great potential as reinforcing agents in polymer nanocomposites in place of synthetic filler particles.<sup>5,9–13</sup>

Despite this promise as the filler phase of nanocomposite materials for infrastructure, transportation, and renewable-energy applications, there are still shortcomings that must be

overcome to achieve optimal performance of CNC–polymer nanocomposites. First, CNCs are largely hydrophilic and can retain large amounts of moisture that have a negative impact on the mechanical properties of resulting nanocomposites.<sup>14,15</sup> Moisture has also been shown to impact CNC–CNC interfacial properties by reducing resistance to interfacial shear.<sup>16–19</sup> Further, during the drying process, significant aggregation of CNCs is observed due to the formation of hydrogen bonds between crystals.<sup>20</sup> Aggregation poses significant problems in the redispersion for effective processing and can lead to nonuniform filler distribution in nanocomposites that is associated with an overall decline in the mechanical performance of the material.<sup>21,22</sup>

A general approach to controlling the interactions between CNCs is via surface modification.<sup>23</sup> Recently, Fox et al. developed an ion-exchange method to further modify sulfated CNC surfaces.<sup>24</sup> These CNCs are extracted from bulk cellulosic materials using sulfuric acid (H<sub>2</sub>SO<sub>4</sub>), and a side esterification reaction occurs at the crystal surface, resulting in hydroxyl

**Received:** December 10, 2017

**Accepted:** February 12, 2018

**Published:** February 12, 2018

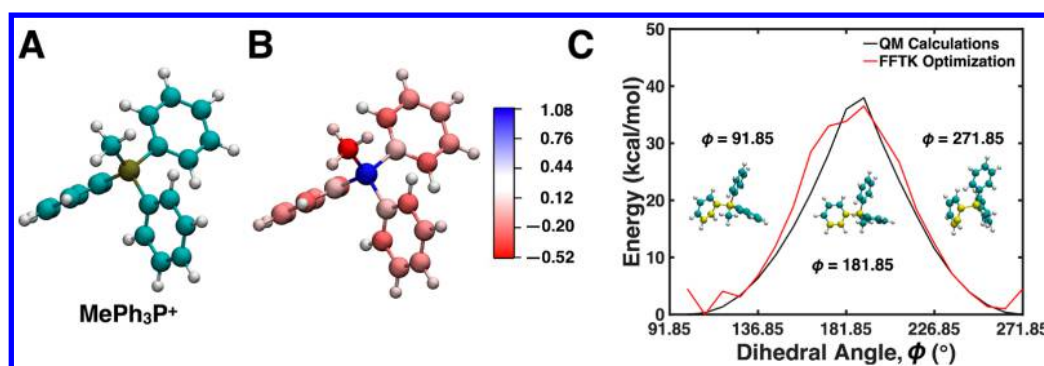


**Figure 1.** (A)  $\text{MePh}_3\text{P}^+$  ionic surface modification that is exchanged for sodium cations on sulfated CNCs. Color codes: cyan = carbon, white = hydrogen, brown = phosphorus. (B) Same cation, color-coded by the atoms' partial charges calculated using the FFTK protocol.<sup>27</sup> Electronegative atoms are shaded red, electropositive atoms are shaded blue, and aliphatic hydrogen atoms are shaded white, with a fixed charge of  $+0.09e$ . (C) Comparison of the energy landscape of the C–C–C–P dihedral (yellow atoms) within  $\text{MePh}_3\text{P}^+$  for a dihedral angle ranging from  $\phi = 91.85^\circ$  to  $\phi = 271.85^\circ$  in steps of  $15^\circ$ . A cutoff of 10 kcal/mol was used in the optimization. The plot shows good agreement between the energy landscapes computed using QM calculations (black line) and the optimized CHARMM dihedral parameters obtained from FFTK (red line).

groups being replaced by sulfate groups.<sup>4,25</sup> These sulfate groups carry a single negative charge that is neutralized by a sodium cation. The sodium cation can subsequently be exchanged for larger, more nonpolar cations, such as methyl-(triphenyl)phosphonium ( $\text{MePh}_3\text{P}^+$ , Figure 1A). Experiments have shown that replacing the sodium cation with  $\text{MePh}_3\text{P}^+$  reduces water adsorption and improves thermal stability of the nanocrystals. Further, these modified CNCs improve filler dispersion when incorporated in polystyrene–CNC nanocomposites.<sup>24</sup> These experimental results demonstrate the tremendous potential of ion-exchanged CNCs for use in CNC-reinforced nanocomposites to overcome current shortcomings in this class of materials. However, a molecular-level understanding of the effects of surface modification is still limited. Computational approaches can provide direct insight into the properties of chemically modified CNC surfaces. With the advent of generalized all-atomistic force fields,<sup>26</sup> these novel chemical modifications can be rapidly parametrized<sup>27</sup> and further characterized using existing simulation techniques.

Here, we investigate the surface and interfacial behaviors of ion-exchanged CNCs using grand-canonical Monte Carlo (GCMC) and steered molecular dynamics (SMD) simulations. The GCMC method<sup>28,29</sup> allows simulation of adsorption at constant temperature and pressure, and has been used extensively in the studies of adsorption on fixed substrates.<sup>30,31</sup>

Here, we employ GCMC simulations combined with molecular dynamics (MD) simulations that take into account the movement of the substrate to study how surface chemistry impacts the water uptake of CNC surfaces at varying relative humidity. In addition to measuring the adsorption isotherm, we also characterize the water distribution, configuration, and dynamics. SMD<sup>32</sup> is a technique by which an external force is applied to a group of atoms, making it possible to effectively simulate atomic force microscopy experiments. We use SMD simulations to probe the traction–separation behavior<sup>33</sup> of CNC–CNC interfaces and to determine how surface chemistry and interfacial moisture influence interfacial failure and mechanics. The experimental characterizations of ion-exchanged CNCs can be found in ref 24.

## 2. MODELS AND METHODS

**2.1. Parametrization of CHARMM Force Field.** In our simulations of surface-modified CNCs, we utilized the CHARMM<sup>34</sup> force field with bond, angle, dihedral, and nonbonded terms (both van

der Waals and electrostatic contributions) with the form of the potential energy function shown in the Supporting Information. We employed parameters from the generalized CHARMM force field<sup>26</sup> and the CHARMM force field for carbohydrates<sup>35–37</sup> for the sulfated CNCs. For the  $\text{MePh}_3\text{P}^+$  ionic surface modification (Figure 1A) we initially intended to use the generalized CHARMM force field, but upon parametrizing the molecule with the CGenFF program<sup>26</sup> (version 3.0.1), we noticed extremely high penalty values (greater than 50) for partial charges as well as bond, angle, and dihedral parameters. As an alternative, we determined the partial charges and structural parameters with high penalty scores using the Force Field Toolkit<sup>27</sup> (FFTK) package implemented in Visual Molecular Dynamics<sup>38</sup> (VMD). FFTK is a protocol that allows rapid parametrization of small molecules using optimization methods that minimize differences between quantum-mechanical (QM) calculations and molecular mechanics (MM) calculations that utilize the CHARMM force field. Figure 1B illustrates the partial charges calculated using this technique. To demonstrate the accuracy of this parametrization technique, Figure 1C shows a comparison between the energy landscapes of the C–C–C–P dihedral calculated using QM relaxed potential energy surface scans and the optimized dihedral parameters from FFTK. The QM calculations were performed using Gaussian09<sup>39</sup> with second-order Møller–Plesset perturbation theory (MP2) and the 6-31G(d) basis set. The full set of parameters used to simulate  $\text{MePh}_3\text{P}^+$  and a more detailed comparison between the QM and MM calculations are provided in the Supporting Information.

**2.2. Combined GCMC and MD Simulations of Water Adsorption.** To study the water adsorption on CNC surfaces, CNCs with two exposed (110) surfaces and dimensions of 10.38 nm along the length of the chain (10 repeat units), 3.31 nm along the width of the crystal (6 chains), and 1.19 nm along the thickness of the crystal (2 layers) were generated using the cellulose-builder tool<sup>40</sup> and the psfgen tool in VMD. On each surface, we replaced 1 out of every 10 hydroxyl groups with a sulfate group and placed the sodium or  $\text{MePh}_3\text{P}^+$  cations adjacent to these groups. The sulfate groups were equally spaced on the surfaces (Figure S1). The CNC was placed in a simulation box with dimensions 10.38 nm  $\times$  3.31 nm  $\times$  8 nm, with periodic boundary conditions in three dimensions (Figure S1).

We performed simulations using the LAMMPS package with a time step of 2 fs. The CNC was first equilibrated using MD for 2 ns in vacuum in the NVT ensemble, where the temperature was kept at  $T = 300$  K by a Langevin thermostat with damping time 100 fs. The backbone carbon atoms of the cellulose chains were tethered to their initial positions by harmonic forces within the CNC surface plane with a spring constant of 10 kcal/(mol  $\text{\AA}^2$ ). After the CNC reached equilibrium, GCMC steps were added to perform exchanges (insertions or deletions) of water molecules with an imaginary ideal-gas reservoir at  $T = 300$  K and a fixed chemical potential. 100 attempts of GCMC exchanges of water molecules, modeled using the rigid

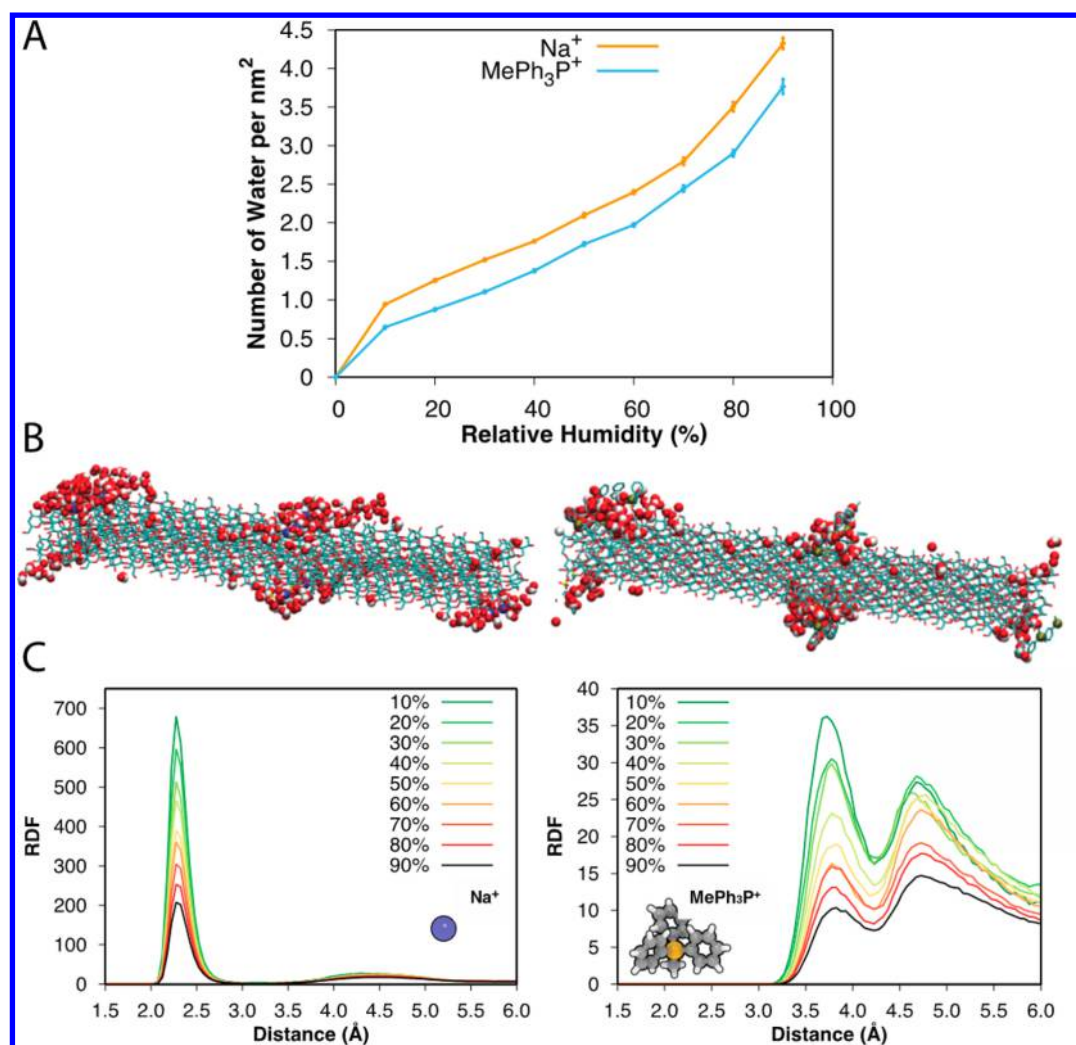


**Figure 2.** (A) Number of adsorbed water molecules per nm<sup>2</sup> as a function of RH for Na-CNC and MePh<sub>3</sub>P-CNC surfaces, obtained from combined GCMC and MD simulations. (B) Representative simulation configurations of adsorbed water on Na-CNC (left) and MePh<sub>3</sub>P-CNC (right) surfaces at RH = 60%. Hydrogen atoms on CNC are not shown for clarity. Color codes: cyan = carbon, red = oxygen, white = hydrogen, yellow = sulfur, blue bead = sodium, brown bead = phosphorus. (C) RDFs of water oxygen atoms around sodium (left) and phosphorus in MePh<sub>3</sub>P<sup>+</sup> (right) at different RH.

TIP3P water model,<sup>41</sup> were performed every 100 fs (every 50 MD steps). At each GCMC step, insertions and deletions attempts were made with equal probability. When inserting a water molecule, its center of mass was placed at a random point within the simulation box. A random orientation was then generated by choosing a random point on a unit sphere, centered around this center of mass, and rotating the water molecule around this axis, over a random angle between 0 and  $2\pi$ . This insertion was accepted or rejected according to the conventional GCMC acceptance criterion. To enable a direct comparison with experiments, where the water mass adsorbed was measured as a function of relative humidity (RH),<sup>24</sup> we related RH to the chemical potential  $\mu$  imposed in the GCMC simulations. RH is defined as the ratio of the partial pressure of water vapor to the saturated vapor pressure. At  $T = 300$  K, the saturated fugacity coefficient of water vapor was measured to be close to 1,<sup>42</sup> so its chemical potential can be approximated by that of an ideal gas. The ideal-gas approximation also applies to the rigid TIP3P water, which has a similar saturated fugacity coefficient.<sup>43</sup> Thus,  $\mu$  is related to RH by  $\mu - \mu_{\text{sat}} = k_{\text{B}}T \ln(\text{RH})$ , where  $\mu_{\text{sat}}$  is the chemical potential of the saturated vapor. We performed GCMC simulations of rigid TIP3P water to obtain  $\mu_{\text{sat}}$  from the measured saturated vapor density of 0.0245 kg/m<sup>3</sup>.<sup>44</sup> Such a low density further supported our ideal-gas approximation as well as the feasibility of GCMC simulations, which were chosen over canonical simulations to better account for water

density fluctuations. With  $\mu_{\text{sat}}$  determined to be  $-10.96$  kcal/mol, we calculated the appropriate  $\mu$  to simulate RH ranging from 10% to 90% (see Table S1).

During the above-mentioned 100 fs between GCMC steps, both the water molecules that were introduced through GCMC steps and the CNC were equilibrated using MD simulations in the NVT ensemble, with the same temperature and thermostat as used in the initial equilibration stage. The MD steps allowed the movement of CNC substrates, which results in a more realistic representation of the experimental system. The combined GCMC/MD simulation ran for 70 ns in total, with the first 10 ns used for the number of water molecules to reach equilibrium and the final 60 ns used for data analysis. During the entire simulation, the bonds and angle of the rigid water molecule were constrained via the SHAKE algorithm.<sup>45</sup> Electrostatic interactions were accounted for through Ewald summation via the particle–particle particle–mesh algorithm with a relative accuracy of  $10^{-4}$ . A cutoff distance of 12 Å was set for the short-range interactions and the real-space contribution to the electrostatic calculations.

**2.3. SMD Simulations of Traction–Separation Behavior.** To understand how water affects the traction–separation behavior of CNC–CNC interfaces with ionic surface modifications, we generated interfaces with the (110) surface exposed (Figure S2) using the tools mentioned in the previous section. CNCs have dimensions of 10.38

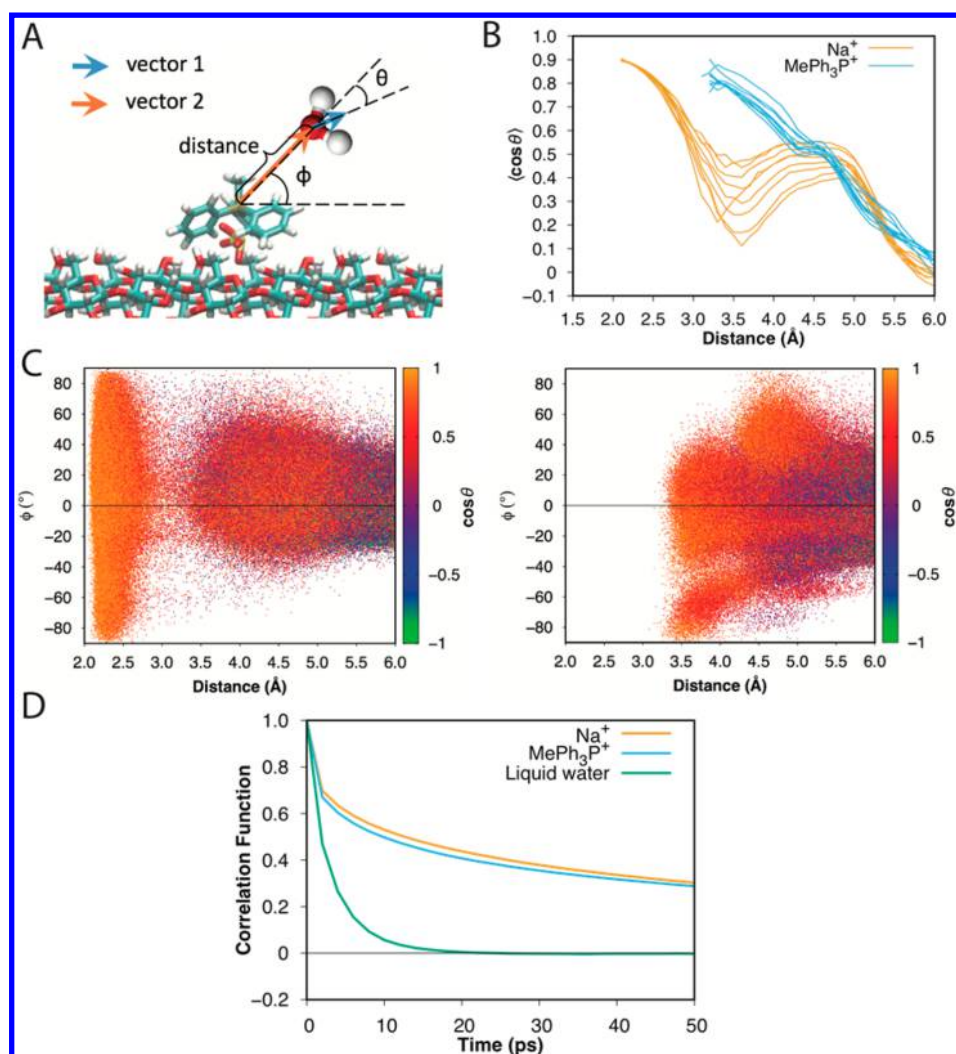


**Figure 3.** (A) Schematic illustration of the distance and angles measured in the simulations to understand orientational ordering of water molecules. (B) Orientational ordering of water molecules as a function of distance to the cations. The nine different curves for each cation correspond to measurements of  $\langle \cos \theta \rangle$  at different RH. (C) Scatter plots of  $\cos \theta$  as a function of distance to the cations and acute angle  $\phi$  for all water molecules in the last 60 ns of simulations at RH = 50%. Left-hand side plot pertains to  $\text{Na}^+$ -CNC surfaces and the right-hand side plot to  $\text{MePh}_3\text{P}^+$ -CNC surfaces. (D) Single-molecule orientational time correlation function for water molecules adsorbed on different CNC surfaces as well as in pure liquid water at a density of 1 g/cm<sup>3</sup>.

nm along the length of the chain (the same as the CNCs used in the water adsorption simulations), 7.50 nm along the width of the crystal (14 chains), and 1.79 nm along the thickness of the crystal (3 layers). Previous work<sup>7</sup> showed that for a finite CNC crystal with width smaller than 14 chains the root-mean-square fluctuation of atoms increased with decreasing crystal width, thereby affecting its mechanical properties. For our traction–separation study, we therefore chose to employ a crystal width of 14 chains to mitigate such finite-size effects. On each exposed CNC surface, the percentage of hydroxyl groups replaced with sulfate groups was again 10%, with a sulfate group distribution pictured in Figure S2. To create interfaces, two CNCs were placed in a simulation box such that the sulfate groups from opposing surfaces were arranged in an interdigitated conformation (Figure S2). Since we are interested in the influence of water on the traction–separation behavior, we studied systems with and without interfacial water (which we refer to as “wet” and “dry” interfaces, respectively). For the wet interface, a single atomic layer of rigid TIP3P water molecules was inserted between the two CNCs using the program packmol.<sup>46</sup> Past experiments,<sup>24</sup> as well as the water adsorption simulations conducted in this study, revealed that  $\text{MePh}_3\text{P}^+$ -modified CNCs adsorb less water than those with sodium cations at the same RH. We choose RH = 90% as a representative case

in the interfacial simulations, corresponding to 616 and 707 water molecules placed at interfaces with  $\text{MePh}_3\text{P}^+$  and sodium cations, respectively, according to our grand-canonical simulations. Periodic boundary conditions were applied along the length ( $x$ -axis in Figure S2) and width ( $z$ -axis) of the crystals, with a nonperiodic boundary normal to the interface ( $y$ -axis).

We performed simulations using the NAMD software package<sup>47</sup> with a time step of 2 fs. First, CNC–CNC interfaces were equilibrated in the  $NVT$  ensemble at  $T = 300$  K for 1.5 ns. During this equilibration, the backbone carbon atoms of the lower crystal were fixed in place while the upper crystal, as well as water in the case of the wet interface, was free to move into contact with the lower crystal to develop the interface. As measured from simulations, in the system with  $\text{MePh}_3\text{P}^+$  cations, the gap between the top and bottom crystal at equilibrium was larger than that in the system with sodium cations, by about 6.48 Å for the dry interface and about 3.68 Å for the wet interface. The larger gap for the  $\text{MePh}_3\text{P}^+$ -modified interface resulted from steric effects arising from the bulky ionic structure. In the presence of water, the difference in gap size decreased because the water increased the gap between CNC crystals with sodium cations by approximately 2.4 Å, whereas it decreased the gap between those with  $\text{MePh}_3\text{P}^+$  cations by approximately 0.4 Å. Once the systems were

equilibrated, we conducted SMD simulations to determine the traction–separation behavior of both dry and wet interfaces. In these simulations, the bottom crystal was again held fixed, and the SMD force was applied to the center of mass of the backbone carbon atoms in the top crystal to simulate interfacial traction and separation, as indicated in Figure S2. The SMD simulations employed a constant pulling velocity of  $2 \times 10^{-5}$  Å/fs and a relatively high SMD spring constant of 4000 kcal/(mol Å<sup>2</sup>) to reduce oscillations of the pulled atoms. These SMD parameters are consistent with our previous studies<sup>16,48</sup> and are appropriate for avoiding any issues associated with rate dependence. An additional discussion on rate dependence is included in the Supporting Information. Five simulations with independent starting configurations were conducted for each case to accurately determine the mechanical properties and changes in free energy<sup>32,49</sup> associated with these interfacial modes of failure.

### 3. RESULTS AND DISCUSSION

**3.1. Water Adsorption on CNC Surfaces.** Figure 2A shows the number of adsorbed water molecules per nm<sup>2</sup> as a function of RH for the two different CNC surfaces studied here. Exchanging the sodium cations with MePh<sub>3</sub>P<sup>+</sup> results in a reduction in water uptake, which is qualitatively consistent with experimental observations.<sup>24</sup> However, due to the difficulty in precisely measuring the surface area per mass of the experimental CNC samples, we are not able to quantitatively compare with experimental measurements,<sup>24</sup> which report water mass adsorbed as a percentage of dried CNC sample mass. A tentative comparison (Figure S3) shows that the simulations and the experiments exhibit quite similar trends as a function of RH. A potential explanation for the observed differences could be that CNCs in the experimental samples are not fully isolated unlike in the simulations.

The qualitative agreement indicates the predictive capability of simulations in terms of relative water uptake ability, which can be exploited to facilitate future design of CNC surface modifications. In addition, the simulations provide deeper insight into the molecular-level structure and dynamics of the adsorbed water near the surfaces. As illustrated in Figure 2B, the adsorbed water molecules tend to aggregate near the cations on the CNC surfaces due to electrostatic interactions that are strong compared to hydrogen bonding with hydroxyl groups on the cellulose chains. To provide a detailed view of the interactions between the water molecules and the cations, we plot the radial distribution functions (RDFs) of water oxygen atoms around the different cations (Figure 2C). The RDFs are computed around the sodium atom for Na-CNCs and the central phosphorus atom in MePh<sub>3</sub>P<sup>+</sup> for MePh<sub>3</sub>P-CNCs. Since the average nearest intercation distance measured from the simulations is  $\sim 11.6$  Å, we plot the RDF within a range of 6 Å, focusing on the water molecules near each cation. For Na-CNC surfaces, the RDFs at different RH show short-distance peaks at  $\sim 2.3$  Å, demonstrating the strong electrostatic interactions between water molecules and sodium cations. These peak values decrease with increasing RH due to the normalization of RDF with respect to an ideal gas. Moreover, the RDF distributions show secondary peaks at  $\sim 4.4$  Å, which arise from the intermolecular hydrogen bonding of water molecules with the first layer of water surrounding the sodium cations. For MePh<sub>3</sub>P-CNC surfaces, the RDFs also display a two-peak profile. Compared to the water distribution near Na-CNC surfaces, where the first layer of water is distributed within 3 Å from the sodium atom, water molecules do not appear closer than 3 Å from the phosphorus atom on MePh<sub>3</sub>P-CNC surfaces. This again can be attributed to the bulky ionic

structure of MePh<sub>3</sub>P<sup>+</sup> disrupting interactions between the water molecules and the phosphorus atom. The RDF distributions still exhibit diminishing peak values with increasing RH due to normalization. The disruption due to the bulky ionic structure and the presence of the nonpolar phenyl groups (Figure 1B) that do not interact favorably with water molecules are the primary contributing factors to the reduced water uptake compared to sodium cations.

**3.2. Orientational Ordering and Dynamics of Water Molecules.** To determine the orientational ordering of water molecules near CNC surfaces, we measure the angle  $\theta$  between two vectors illustrated in Figure 3A: vector 1 aligned with the water dipole moment, i.e., pointing from the water oxygen atom to the center of the two hydrogen atoms, and vector 2 pointing from the sodium atom or the phosphorus atom in MePh<sub>3</sub>P<sup>+</sup> to the water oxygen atom. A positive value of  $\cos \theta$  corresponds to the water dipole moment pointing away from the cation, while a negative value indicates that it is directed toward the cation. Figure 3B shows  $\langle \cos \theta \rangle$  as a function of the distance between the water oxygen atom and the cations at different RH. Figure 3C provides scatter plots of  $\cos \theta$  as a function of the same distance and the acute angle  $\phi$  formed by vector 2 and the horizontal plane (cf. Figure 3A). The points represent the configurations of all water molecules in the last 60 ns of simulations at RH = 50%. For Na-CNC surfaces, the  $\langle \cos \theta \rangle$  plots (Figure 3B) show two positive peaks at positions corresponding to the peak positions in the RDF plots (Figure 2C). In these two regions, most water molecules are oriented with their partially negatively charged oxygen atoms pointing toward the sodium cations. Such ordering is primarily due to the electrostatic interaction between water and sodium cation as well as the water–water hydrogen bonding discussed in the previous section. The negatively charged sulfate groups will also affect the orientation of nearby water molecules by attracting the partially positive charged hydrogen atoms. Water molecules within 3 Å from the sodium atom can explore a large range of angles  $\phi$ , while the ones located further away are more concentrated above the horizontal plane of the sodium atoms with weaker orientational ordering. For MePh<sub>3</sub>P-CNC surfaces, consistent with the RDF plots, the water molecules appear at a larger distance, but they are still oriented with their oxygen atoms pointing toward the phosphorus atoms at those separations. Because of the disruption caused by the ionic structure of MePh<sub>3</sub>P<sup>+</sup>, a certain range of angles  $\phi$  (e.g.,  $\phi > 60^\circ$ ) is prohibited for water molecules closer than  $\sim 4.3$  Å.

To understand how cation chemistry affects the orientational dynamics of water molecules, we perform canonical simulations at RH = 70%, where the number of water molecules is determined from GCMC simulations. We calculate the single-molecule orientational time correlation function

$$C(t) = \frac{\langle \langle \mathbf{u}(t_0)\mathbf{u}(t_0 + t) \rangle \rangle - \langle \mathbf{u}(t_0) \rangle \langle \mathbf{u}(t_0 + t) \rangle \rangle_N}{C(0)} \quad (1)$$

where  $\mathbf{u}(t)$  is vector 1 defined in Figure 3A for each water molecule at time  $t$  and the angular brackets represent an ensemble average over times  $t_0$  and over all  $N$  water molecules. We consider all the water molecules as adsorbed in our calculations due to the sufficiently low detachment probability of water molecules. (For the Na-CNC surface, at most one water molecule detaches at any time out of the total 192 water molecules, and we only observe detached water molecules for  $\sim 0.63$  ns during the 8 ns simulations.) Figure 3D illustrates the

correlation function vs time for water molecules adsorbed on the two different CNC surfaces as well as that of a pure water system at a density of 1 g/cm<sup>3</sup>. These results show that the orientational relaxation of water adsorbed on the surface is much slower than even in bulk water at the same temperature. Furthermore, the correlation function for water on the MePh<sub>3</sub>P-CNC surface decreases slightly faster than that on the Na-CNC surface, indicating that sodium cations impose slightly stronger constraints on the orientational relaxation of water molecules.

**3.3. Separation of CNC–CNC Interfaces.** We use separation simulations to determine several important interfacial mechanical properties, including interfacial adhesion energy as well as interfacial stiffness and strength. We first measure the separation force–displacement curves and then calculate the interfacial adhesion energy by integrating these curves and taking an exponential average of five independent trajectories. The force–displacement curves and the interfacial adhesion energies for dry and wet interfaces are shown for Na-CNCs in Figure 4A and for MePh<sub>3</sub>P-CNCs in Figure 4B. For the force–displacement curves, a separation distance of zero corresponds to the equilibrated configuration of the CNC surfaces determined in the Models and Methods section.

There are several interesting trends in the interfacial adhesion energy. For the dry interface, the adhesion energy is greatly decreased when sodium cations are replaced with MePh<sub>3</sub>P<sup>+</sup> cations. As discussed in our previous study,<sup>24</sup> the larger MePh<sub>3</sub>P<sup>+</sup> cation decreases interfacial adhesion by physically increasing the distance between the two CNCs, which prevents hydrogen bonding across the interface and simultaneously reduces van der Waals interactions. Furthermore, we observe opposing trends for different surface chemistries when water is introduced at the interface. For the interface with MePh<sub>3</sub>P<sup>+</sup> cations, the interfacial adhesion energy increases by ~106% when water is introduced, but the energy decreases by ~16% for the interface with sodium cations. As the interfaces are separated, water molecules can either stay in close contact with the individual surfaces or maintain contact with other water molecules to form capillary bridges<sup>50,51</sup> between the surfaces. The simulation snapshots in Figures 4A and 4B show that for the same interfacial separation of 3 nm, as determined from the distance between hydroxyl groups on the top and bottom CNC surfaces, the MePh<sub>3</sub>P<sup>+</sup> interface exhibits more capillary bridges (a maximum of six bridges; note that not all of them are clearly visible in the side view snapshots) than the sodium interface (a maximum of three bridges). This can be attributed to the higher concentration of water molecules around the MePh<sub>3</sub>P<sup>+</sup> cations at the interface, as illustrated in the top view of the interfaces at equilibrium configurations in Figures 4A and 4B. In addition, water–water interactions are more favorable than interactions between water and any of the three nonpolar phenyl groups of a MePh<sub>3</sub>P<sup>+</sup> cation, which further promotes the formation of capillary bridges. As discussed in our previous study<sup>16</sup> and illustrated in the force–displacement curves for MePh<sub>3</sub>P<sup>+</sup> in Figure 4B, these capillary bridges serve to increase the adhesive force between surfaces as well as the interfacial failure strain.

For sodium interfaces (Figure 4A), even though the formation of capillary bridges leads to a small increase in adhesive force at large separation distance (>6 Å), the adhesion energy decreases in the presence of water, primarily because water molecules disrupt hydrogen bonds between hydroxyl group on closely separated CNC surfaces. Instead, these

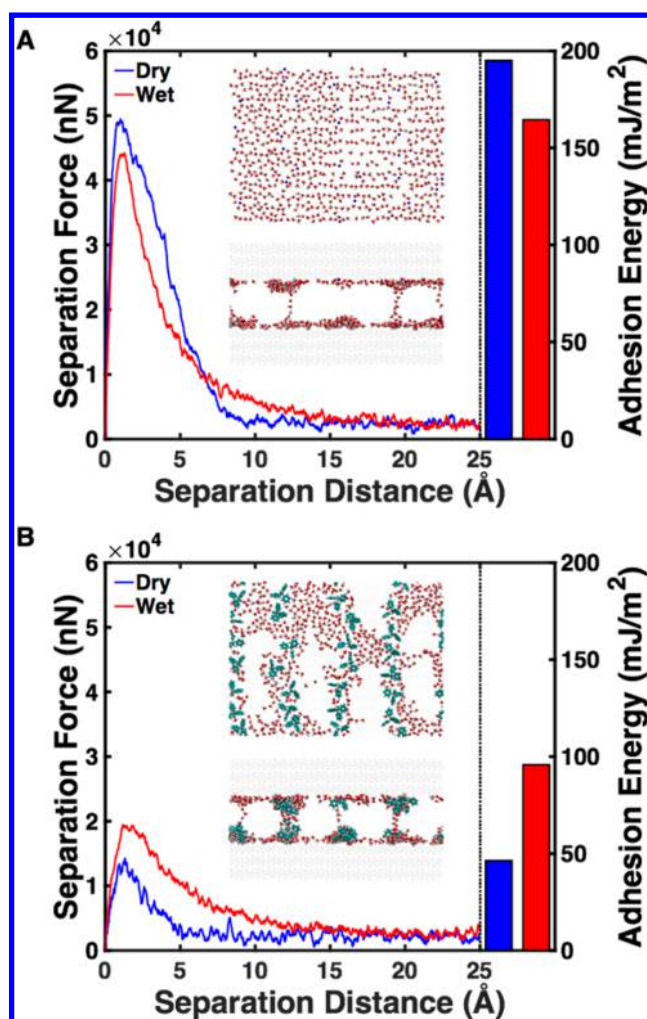


**Figure 4.** Force–displacement curves and interfacial adhesion energies for the separation of CNC–CNC interfaces averaged over five independent starting configurations for (A) Na-CNCs and (B) MePh<sub>3</sub>P-CNCs. Blue data points/bars correspond to the dry interface, and red data/bars correspond to the wet interface. The adhesion energy is calculated by integrating the individual force–displacement curves and taking the exponential average to obtain the energy difference between the equilibrated state and the fully separated state (separation distance of 3 nm). Insets are top and side views of the water distribution at CNC–CNC interfaces. Color codes are the same as in Figure 2. In the top view, we only show the cations at both surfaces and water molecules. The aggregation of water molecules around MePh<sub>3</sub>P<sup>+</sup> modifications leads to an increased formation of capillary bridges between CNC surfaces.

hydroxyl–hydroxyl hydrogen bonds between CNC surfaces are replaced by water–hydroxyl hydrogen bonds. These water–hydroxyl hydrogen bonds exhibit lower occupancy, i.e., the percentage of time that hydrogen bonds between two residues (e.g., glucose unit, water molecule) are within the cutoff criteria in a canonical simulation (see Figure S4). Lower occupancy corresponds to more unstable, fleeting hydrogen bonds compared to hydroxyl–hydroxyl hydrogen bonds with high occupancy. The collective decrease in stability of the molecular interactions leads to a decrease in the interfacial adhesion. Our simulation results parallel recent experimental findings<sup>24</sup> for the surface energies of surface-modified CNCs. In those experiments, the surface energy of Na-CNCs decreases at RH = 50%

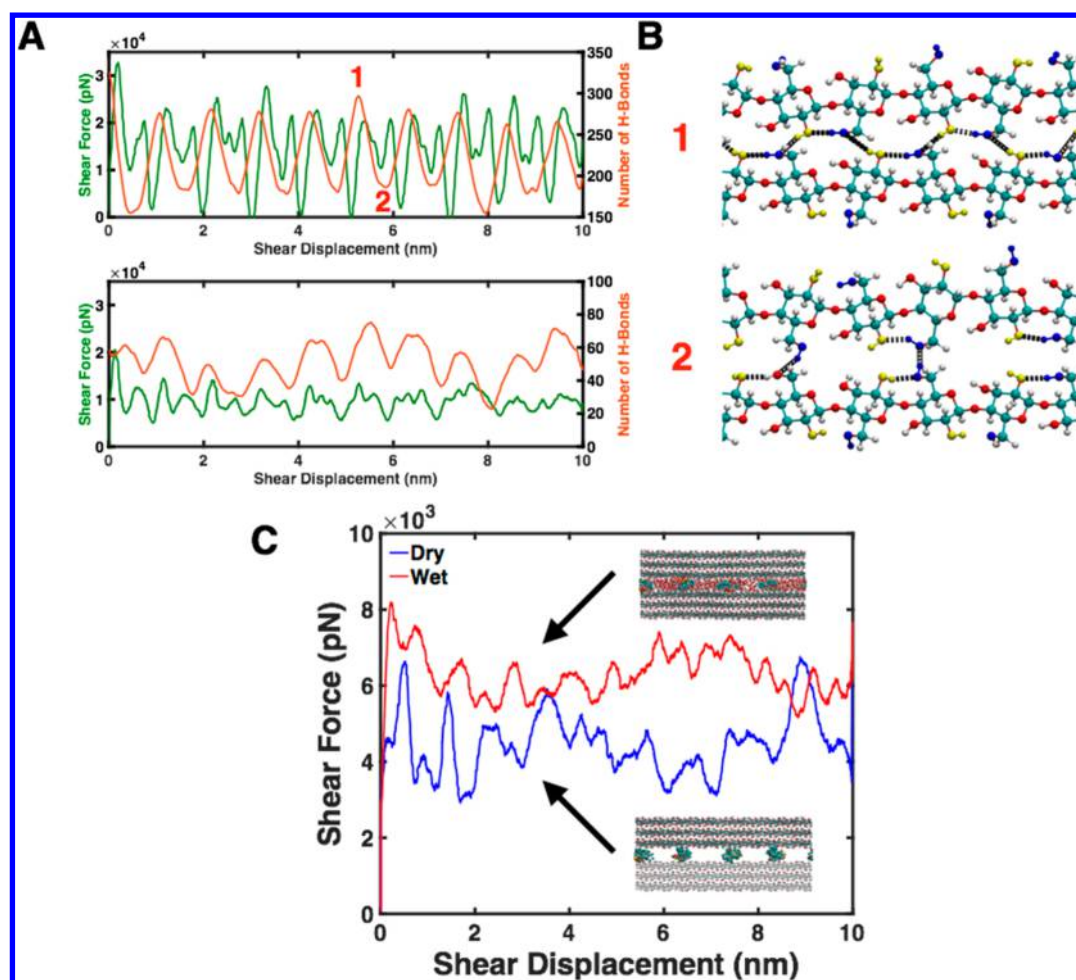


**Figure 5.** (A) Force–displacement curves (green lines) for the CNC–CNC interface with sodium cations under shear deformation both in the absence (top) and presence (bottom) of moisture. The numbers of CNC–CNC hydrogen bonds formed across the interface (orange lines) are overlaid on these curves to demonstrate how the force–displacement behavior is governed by breaking hydrogen bonds. (B) Illustration of the hydrogen-bond network formed across the interface. A maximum number of hydrogen bonds (location 1 in part A) is formed when C6 hydroxyls (blue atoms) interact with C2 hydroxyls (yellow atoms) across the interface; a minimum (location 2 in part A) is observed when these hydroxyls interact with the identical hydroxyls across the interface. (C) Force–displacement curves for the CNC–CNC interface with MePh<sub>3</sub>P<sup>+</sup> cations under shear deformation in both the absence and presence of moisture.

compared to dry samples, whereas the surface energy of MePh<sub>3</sub>P–CNCs increases.

**3.4. Shear of CNC–CNC Interfaces.** Traction simulations at a constant interfacial separation distance can reveal how different interfacial chemistries respond to the presence of water under shear deformation. We choose a separation distance of zero (i.e., equilibrium gap) for both interfaces in our study. For the dry interface with sodium cations, an oscillatory, periodic shape is observed for the shear force–displacement curves (top panel in Figure 5A). The force peaks display a periodicity of  $\sim 5.2$  Å, corresponding to the size of one glucose unit along the cellulose chain backbone. We also observe two distinct types of shearing events that can be explained by examining the hydrogen bonds and alignment of glucose units across the interface. The first type of event, corresponding to a force barrier (i.e., difference between force maximum and minimum) of 20–30 nN, is consistent with the breaking of numerous hydrogen bonds across the interface. We verify this mechanism by tracking the number of hydrogen bonds formed between cellulose chains across the interface. As shown in Figure 5A, the temporal locations of the large force barriers slightly lag the maximum values in the number of

hydrogen bonds (e.g., location 1) when C6 hydroxyls (blue atoms in Figure 5B) are aligned with C2 hydroxyls (yellow atoms in Figure 5B) on the opposing CNC surface. In contrast, the second type of shearing event has a lower force barrier of 10–15 nN and corresponds to the positions where the number of hydrogen bonds is minima (e.g., location 2). Here, C6 and C2 hydroxyls interact with their identical counterpart across the interface (Figure 5B) and form fewer hydrogen bonds, resulting in lower force barriers to shear displacement.

When water is added at the interface at RH = 90%, the maximum shear force barrier is significantly decreased to 5–10 nN (Figure 5A, bottom panel). This suggests that water serves as a lubricating agent and reduces interfacial sliding friction between the two surfaces. Additionally, we observe a similar oscillatory shape of the force–displacement curve to that of the dry interface, indicating that a hydrogen bond network is maintained across the interface. However, the number of CNC–CNC hydrogen bonds decreases significantly (Figure 5A), which is accompanied by the development of a CNC–water–CNC hydrogen bonding network across the interface. This network also contributes to the interfacial shear strength but is significantly weaker than the network formed at a dry

interface due to the lower stability of CNC–water hydrogen bonds discussed above in the context of interfacial separation.

The behavior of the  $\text{MePh}_3\text{P}^+$  interface is quite different. While there is still some indication of periodicity, the force barriers are significantly smaller than those for Na-CNCs (Figure 5C), as is to be expected for an interface at which hydrogen bonds are suppressed due to the large separation between CNC hydroxyl groups. During shear deformation, the two opposing surfaces interact through relatively weaker nonbonded (electrostatic and van der Waals) interactions.<sup>24</sup> When water is added at this interface, the interfacial shear force is increased. This reversal in trend can be explained by the development of a water-mediated hydrogen bonding network between the surfaces due to surface amphiphilicity. As seen in Figure 4B, the introduction of  $\text{MePh}_3\text{P}^+$  leads to clear hydrophobic patches at the ionic modification sites besides the hydrophilic patches of unmodified hydroxyl-rich CNC. The cation locations are considered to be effectively hydrophobic due to the presence of the nonpolar phenyl groups that do not interact favorably with water molecules. Therefore, water molecules do not fill into the spaces between  $\text{MePh}_3\text{P}^+$  cations and the opposing CNC surface to provide a lubricating effect. Instead, water here serves to bridge the hydrophilic patches on opposing surfaces. In the dry case, these hydrophilic regions are physically separated due to the bulky ionic structure, but when water is introduced, it partially fills the empty space as shown in the simulation snapshots in Figures 4B and 5C. In doing so, the interface exhibits increased resistance to shear deformation via the newly developed water-mediated hydrogen bonding network between the surfaces.

#### 4. CONCLUSIONS

We have employed atomistic GCMC and SMD simulations to study water adsorption and interfacial mechanics of surface-modified CNCs. Consistent with experimental dynamic vapor sorption measurements, we found that  $\text{MePh}_3\text{P}^+$ -exchanged CNCs have lower water uptake than Na-CNCs, which we explain to be primarily due to the disruption arising from the bulky ionic structure of  $\text{MePh}_3\text{P}^+$ . The adsorbed water accumulates near the cations and tends to be oriented with its oxygen atoms pointing toward the cations. Such orientational ordering arises mostly from the electrostatic interactions as well as water–water hydrogen bonding. We also found that the single-molecule orientational dynamics of adsorbed water is much slower than that of liquid water.

Traction–separation behavior of these interfaces is highly dependent on the surface chemistry. In the dry state, introducing the larger  $\text{MePh}_3\text{P}^+$  cation in place of sodium cations reduces interfacial adhesion and shear resistance by increasing the distance between CNC hydroxyl groups at the interface. In the presence of water, Na-CNCs exhibit decreased adhesion energy and shear resistance as hydrogen bonds between hydroxyl groups are largely replaced by water–hydroxyl hydrogen bonds that have lower occupancy and thereby degrade interfacial mechanical properties. On the other hand, in this case,  $\text{MePh}_3\text{P}^+$ -exchanged CNCs exhibit increased adhesion energy and interfacial shear resistance due to capillary water bridges or water-mediated hydrogen bond networks developed between surfaces. Interestingly, even though we introduce surface modification that is ionic in nature, the  $\text{MePh}_3\text{P}^+$  cations serve to change the interface such that it exhibits behaviors (formation of capillary bridges, enhancement

of mechanical properties upon wetting) indicative of a hydrophobic interface.<sup>16</sup>

In this study, we have shown that chemical surface modification is a viable option for changing the adsorption and traction–separation behavior of CNC. These results are an important first step toward the design of moisture-tolerant CNC–polymer nanocomposites. While we have specifically assessed how  $\text{MePh}_3\text{P}^+$  reduces water adsorption and enhances the water tolerance of interfacial mechanical properties, our computational approach can be easily adapted to rapidly evaluate other chemical modifications. These techniques not only provide atomistic insight into the surface and interfacial properties of CNCs but also suggest strategies for further tuning these properties to facilitate improved industrial design of CNC–polymer nanocomposites with enhanced moisture tolerance.

#### ■ ASSOCIATED CONTENT

##### Supporting Information

The Supporting Information is available free of charge on the ACS Publications website at DOI: 10.1021/acsami.7b18803.

Parametrization, force field parameters, pulling rate dependence, initial simulation configurations, comparison of computational and experimental trends of water adsorption, hydrogen-bond occupancy, chemical potential at different relative humidities (PDF)

#### ■ AUTHOR INFORMATION

##### Corresponding Author

\*E-mail: [luijten@northwestern.edu](mailto:luijten@northwestern.edu) (E.L.).

##### ORCID

Erik Luijten: 0000-0003-2364-1866

##### Present Address

R.S.: Department of Mechanical Engineering, Northern Illinois University, DeKalb, IL 60115.

##### Author Contributions

Z.W. and R.S. contributed equally.

##### Funding

All authors received funding from the U.S. Department of Commerce, National Institute of Standards and Technology, as part of the Center for Hierarchical Materials Design (CHiMaD) under Award No. 70NANB14H012. S.K. and R.S. acknowledge support from an Office of Naval Research Early Career Award (PECASE # N00014-16-1-3175).

##### Notes

The authors declare no competing financial interest.

#### ■ ACKNOWLEDGMENTS

We thank Douglas M. Fox and Jeffrey W. Gilman for useful discussions and providing experimental data. The authors acknowledge support through supercomputing grants from Northwestern University's Quest High Performance Computing Center as well as the Department of Defense HPC System.

#### ■ REFERENCES

- (1) Klemm, D.; Heublein, B.; Fink, H. P.; Bohn, A. Cellulose: Fascinating Biopolymer and Sustainable Raw Material. *Angew. Chem., Int. Ed.* **2005**, *44*, 3358–3393.
- (2) Bondeson, D.; Mathew, A.; Oksman, K. Optimization of the Isolation of Nanocrystals from Microcrystalline Cellulose by Acid Hydrolysis. *Cellulose* **2006**, *13*, 171–180.

- (3) Filson, P. B.; Dawson-Andoh, B. E.; Schwegler-Berry, D. Enzymatic-Mediated Production of Cellulose Nanocrystals from Recycled Pulp. *Green Chem.* **2009**, *11*, 1808–1814.
- (4) Camarero Espinosa, S.; Kuhnt, T.; Foster, E. J.; Weder, C. Isolation of Thermally Stable Cellulose Nanocrystals by Phosphoric Acid Hydrolysis. *Biomacromolecules* **2013**, *14*, 1223–1230.
- (5) Moon, R. J.; Martini, A.; Nairn, J.; Simonsen, J.; Youngblood, J. Cellulose Nanomaterials Review: Structure, Properties and Nanocomposites. *Chem. Soc. Rev.* **2011**, *40*, 3941–3994.
- (6) Nishiyama, Y.; Langan, P.; Chanzy, H. Crystal Structure and Hydrogen-bonding System in Cellulose I $\beta$  from Synchrotron X-ray and Neutron Fiber Diffraction. *J. Am. Chem. Soc.* **2002**, *124*, 9074–9082.
- (7) Sinko, R.; Mishra, S.; Ruiz, L.; Brandis, N.; Ketten, S. Dimensions of Biological Cellulose Nanocrystals Maximize Fracture Strength. *ACS Macro Lett.* **2014**, *3*, 64–69.
- (8) Tashiro, K.; Kobayashi, M. Theoretical Evaluation of Three-Dimensional Elastic Constants of Native and Regenerated Celluloses: Role of Hydrogen Bonds. *Polymer* **1991**, *32*, 1516–1530.
- (9) Favier, V.; Chanzy, H.; Cavaille, J. Y. Polymer Nanocomposites Reinforced by Cellulose Whiskers. *Macromolecules* **1995**, *28*, 6365–6367.
- (10) Beecher, J. F. Organic Materials: Wood, Trees and Nanotechnology. *Nat. Nanotechnol.* **2007**, *2*, 466–467.
- (11) Svagan, A. J.; Samir, M. A. S. A.; Berglund, L. A. Biomimetic Foams of High Mechanical Performance Based on Nanostructured Cell Walls Reinforced by Native Cellulose Nanofibrils. *Adv. Mater.* **2008**, *20*, 1263–1269.
- (12) Habibi, Y.; Dufresne, A. Highly Filled Bionanocomposites from Functionalized Polysaccharide Nanocrystals. *Biomacromolecules* **2008**, *9*, 1974–1980.
- (13) Dong, H.; Strawhecker, K. E.; Snyder, J. F.; Orlicki, J. A.; Reiner, R. S.; Rudie, A. W. Cellulose Nanocrystals as a Reinforcing Material for Electrospun Poly(methyl methacrylate) Fibers: Formation, Properties and Nanomechanical Characterization. *Carbohydr. Polym.* **2012**, *87*, 2488–2495.
- (14) Nogueira, P.; Ramirez, C.; Torres, A.; Abad, M. J.; Cano, J.; Lopez, J.; Lopez-Bueno, I.; Barral, L. Effect of Water Sorption on the Structure and Mechanical Properties of an Epoxy Resin System. *J. Appl. Polym. Sci.* **2001**, *80*, 71–80.
- (15) Dagnon, K. L.; Shanmuganathan, K.; Weder, C.; Rowan, S. J. Water-Triggered Modulus Changes of Cellulose Nanofiber Nanocomposites with Hydrophobic Polymer Matrices. *Macromolecules* **2012**, *45*, 4707–4715.
- (16) Sinko, R.; Ketten, S. Effect of Moisture on the Traction-Separation Behavior of Cellulose Nanocrystal Interfaces. *Appl. Phys. Lett.* **2014**, *105*, 243702.
- (17) Sinko, R.; Qin, X.; Ketten, S. Interfacial mechanics of cellulose nanocrystals. *MRS Bull.* **2015**, *40*, 340–348.
- (18) Dagnon, K. L.; Shanmuganathan, K.; Weder, C.; Rowan, S. J. Water-Triggered Modulus Changes of Cellulose Nanofiber Nanocomposites with Hydrophobic Polymer Matrices. *Macromolecules* **2012**, *45*, 4707–4715.
- (19) Capadona, J. R.; Shanmuganathan, K.; Tyler, D. J.; Rowan, S. J.; Weder, C. Stimuli-Responsive Polymer Nanocomposites Inspired by the Sea Cucumber Dermis. *Science* **2008**, *319*, 1370–1374.
- (20) Phan-Xuan, T.; Thuresson, A.; Skepö, M.; Labrador, A.; Bordes, R.; Matic, A. Aggregation behavior of aqueous cellulose nanocrystals: the effect of inorganic salts. *Cellulose* **2016**, *23*, 3653–3663.
- (21) Song, Y. S.; Youn, J. R. Influence of Dispersion States of Carbon Nanotubes on Physical Properties of Epoxy Nanocomposites. *Carbon* **2005**, *43*, 1378–1385.
- (22) Tingaut, P.; Zimmermann, T.; Lopez-Suevos, F. Synthesis and Characterization of Bionanocomposites with Tunable Properties from Poly(lactic acid) and Acetylated Microfibrillated Cellulose. *Biomacromolecules* **2010**, *11*, 454–464.
- (23) Habibi, Y.; Lucia, L. A.; Rojas, O. J. Cellulose Nanocrystals: Chemistry, Self-Assembly, and Applications. *Chem. Rev.* **2010**, *110*, 3479–3500.
- (24) Fox, D. M.; Rodriguez, R. S.; Devilbiss, M. N.; Woodcock, J.; Davis, C. S.; Sinko, R.; Ketten, S.; Gilman, J. W. Simultaneously Tailoring Surface Energies and Thermal Stabilities of Cellulose Nanocrystals Using Ion Exchange: Effects on Polymer Composite Properties for Transportation, Infrastructure, and Renewable Energy Applications. *ACS Appl. Mater. Interfaces* **2016**, *8*, 27270–27281.
- (25) Lu, P.; Hsieh, Y. L. Preparation and Properties of Cellulose Nanocrystals: Rods, Spheres, and Network. *Carbohydr. Polym.* **2010**, *82*, 329–336.
- (26) Vanommeslaeghe, K.; Hatcher, E.; Acharya, C.; Kundu, S.; Zhong, S.; Shim, J.; Darian, E.; Guvench, O.; Lopes, P.; Vorobyov, I.; MacKerell, A. D. CHARMM General Force Field: A Force Field for Drug-Like Molecules Compatible with the CHARMM All-Atom Additive Biological Force Fields. *J. Comput. Chem.* **2009**, *31*, 671–690.
- (27) Mayne, C. G.; Saam, J.; Schulten, K.; Tajkhorshid, E.; Gumbart, J. C. Rapid Parameterization of Small Molecules Using the Force Field Toolkit. *J. Comput. Chem.* **2013**, *34*, 2757–2770.
- (28) Norman, G. E.; Filinov, V. S. Investigations of Phase Transitions by a Monte-Carlo Method. *High Temp.* **1969**, *7*, 216.
- (29) Adams, D. J. Grand Canonical Ensemble Monte-Carlo for a Lennard-Jones Fluid. *Mol. Phys.* **1975**, *29*, 307–311.
- (30) Nicholson, D.; Parsonage, N. G. *Computer Simulation and the Statistical Mechanics of Adsorption*; Academic Press: 1982.
- (31) Smit, B. Grand Canonical Monte Carlo Simulations of Chain Molecules: Adsorption Isotherms of Alkanes in Zeolites. *Mol. Phys.* **1995**, *85*, 153–172.
- (32) Park, S.; Khalili-Araghi, F.; Tajkhorshid, E.; Schulten, K. Free Energy Calculation from Steered Molecular Dynamics Simulations Using Jarzynski's Equality. *J. Chem. Phys.* **2003**, *119*, 3559–3566.
- (33) Park, K.; Paulino, G. H. Cohesive Zone Models: A Critical Review of Traction-Separation Relationships Across Fracture Surfaces. *Appl. Mech. Rev.* **2011**, *64*, 060802.
- (34) Brooks, B. R.; Bruccoleri, R. E.; Olafson, B. D.; States, D. J.; Swaminathan, S.; Karplus, M. Charmm: A Program for Macromolecular Energy, Minimization, and Dynamics Calculations. *J. Comput. Chem.* **1983**, *4*, 187–217.
- (35) Grootenhuys, P. D. J.; Haasnoot, C. A. G. A Charmm Based Force Field for Carbohydrates Using the CHEAT Approach: Carbohydrate Hydroxyl Groups Represented by Extended Atoms. *Mol. Simul.* **1993**, *10*, 75–95.
- (36) Ha, S. N.; Giammona, A.; Field, M.; Brady, J. W. A Revised Potential-Energy Surface for Molecular Mechanics Studies of Carbohydrates. *Carbohydr. Res.* **1988**, *180*, 207–221.
- (37) Raman, E. P.; Guvench, O.; MacKerell, A. D. CHARMM Additive All-Atom Force Field for Glycosidic Linkages in Carbohydrates Involving Furanoses. *J. Phys. Chem. B* **2010**, *114*, 12981–12994.
- (38) Humphrey, W.; Dalke, A.; Schulten, K. VMD: Visual Molecular Dynamics. *J. Mol. Graphics* **1996**, *14*, 33–38.
- (39) Frisch, M. J.; Trucks, G. W.; Schlegel, H. B.; Scuseria, G. E.; Robb, M. A.; Cheeseman, J. R.; Scalmani, G.; Barone, V.; Mennucci, B.; Petersson, G. A.; Nakatsuji, H.; Caricato, M.; Li, X.; Hratchian, H. P.; Izmaylov, A. F.; Bloino, J.; Zheng, G.; Sonnenberg, J. L.; Hada, M.; Ehara, M.; Toyota, K.; Fukuda, R.; Hasegawa, J.; Ishida, M.; Nakajima, T.; Honda, Y.; Kitao, O.; Nakai, H.; Vreven, T.; Montgomery, J. A., Jr.; Peralta, J. E.; Ogliaro, F.; Bearpark, M.; Heyd, J. J.; Brothers, E.; Kudin, K. N.; Staroverov, V. N.; Kobayashi, R.; Normand, J.; Raghavachari, K.; Rendell, A.; Burant, J. C.; Iyengar, S. S.; Tomasi, J.; Cossi, M.; Rega, N.; Millam, J. M.; Klene, M.; Knox, J. E.; Cross, J. B.; Bakken, V.; Adamo, C.; Jaramillo, J.; Gomperts, R.; Stratmann, R. E.; Yazyev, O.; Austin, A. J.; Cammi, R.; Pomelli, C.; Ochterski, J. W.; Martin, R. L.; Morokuma, K.; Zakrzewski, V. G.; Voth, G. A.; Salvador, P.; Dannenberg, J. J.; Dapprich, S.; Daniels, A. D.; Farkas, Ö.; Foresman, J. B.; Ortiz, J. V.; Cioslowski, J.; Fox, D. J. *Gaussian 09*, Revision D.01; Gaussian, Inc.: Wallingford, CT, 2009.
- (40) Gomes, T. C. F.; Skaf, M. S. Cellulose-Builder: A Toolkit for Building Crystalline Structures of Cellulose. *J. Comput. Chem.* **2012**, *33*, 1338–1346.

- (41) Jorgensen, W. L. Pressure Dependence of the Structure and Properties of Liquid N-Butane. *J. Am. Chem. Soc.* **1981**, *103*, 4721–4726.
- (42) Keenan, J. H.; Keyes, F. G.; Hill, P. G.; Moore, J. G. *Steam Tables: Thermodynamic Properties of Water Including Vapor, Liquid, and Solid Phases*, 1st ed.; Wiley: 1969.
- (43) Wierchowski, S. J.; Kofke, D. A. Fugacity Coefficients of Saturated Water from Molecular Simulation. *J. Phys. Chem. B* **2003**, *107*, 12808–12813.
- (44) Vega, C.; de Miguel, E. Surface Tension of the Most Popular Models of Water by using the Test-Area Simulation Method. *J. Chem. Phys.* **2007**, *126*, 154707.
- (45) Ryckaert, J. P.; Ciccotti, G.; Berendsen, H. J. C. Numerical Integration of Cartesian Equations of Motion of a System with Constraints: Molecular Dynamics of N-Alkanes. *J. Comput. Phys.* **1977**, *23*, 327–341.
- (46) Martinez, L.; Andrade, R.; Birgin, E. G.; Martinez, J. M. PACKMOL: A Package for Building Initial Configurations for Molecular Dynamics Simulations. *J. Comput. Chem.* **2009**, *30*, 2157–2164.
- (47) Phillips, J. C.; Braun, R.; Wang, W.; Gumbart, J.; Tajkhorshid, E.; Villa, E.; Chipot, C.; Skeel, R. D.; Kale, L.; Schulten, K. Scalable Molecular Dynamics with NAMD. *J. Comput. Chem.* **2005**, *26*, 1781–1802.
- (48) Sinko, R.; Keten, S. Traction-Separation Laws and Stick-Slip Shear Phenomenon of Interfaces between Cellulose Nanocrystals. *J. Mech. Phys. Solids* **2015**, *78*, 526–539.
- (49) Jarzynski, C. Nonequilibrium Equality for Free Energy Differences. *Phys. Rev. Lett.* **1997**, *78*, 2690–2693.
- (50) Rabinovich, Y. I.; Esayanur, M. S.; Moudgil, B. M. Capillary Forces Between Two Spheres with a Fixed Volume Liquid Bridge: Theory and Experiment. *Langmuir* **2005**, *21*, 10992–10997.
- (51) Dormann, M.; Schmid, H. J. Simulation of Capillary Bridges between Nanoscale Particles. *Langmuir* **2014**, *30*, 1055–1062.